

CoNi-Layered Double Hydroxides Electrodes with Hierarchical Structure and Dual-Ion Doping for High-Performance Asymmetric Supercapacitors

Mingjiao Shao, Qiyuan Wu, Yang Yang, Fengfeng Li, Hongwei Sheng, Jiao Yuan, Huasheng Bi, Yuqi Ma, Haoshuo Zhang, Guomei Tang,* and Wei Lan*

The agglomeration caused by high loading and the blockage of electrolyte ion transport are the main bottleneck problems that limit the application of layered double hydroxide (LDH) materials. Here, a hierarchically structured CuO@CoNi-LDH composite is constructed on a copper foam (CF) scaffold, with alkali/halogen dual-ion codoping employed to synergistically enhance its electrochemical performance. The CF/CuO core provides a conductive backbone for high-loading LDH, while Li⁺ optimizes the electronic structure. The Br⁻ ion with multiple effects can reduce the OH⁻ adsorption energy and strengthen the covalent characteristics of Co/Ni-O in the LDH, thereby improving reaction

activity. The hierarchical architecture combined with the ionic size effect facilitates charge transport and ion diffusion, enabling the LDH_(Li,Br) electrode to deliver a high areal capacitance of 45.9 F cm⁻² at 5 mA cm⁻² and still retain 56% of its initial capacitance after 14 000 cycles under a high mass loading of 16 mg cm⁻². An asymmetric supercapacitor using CF/CuO@CoNi-LDH(LiBr)//AC exhibits excellent performance (1.87 F cm⁻² at 5 mA cm⁻², 55.6% retention at 30 mA cm⁻²), stable cycling (89.15% after 6400 cycles), and high energy density (0.67 mWh cm⁻²), highlighting the practical potential of dual-ion doping and hierarchical design.

1. Introduction

Supercapacitors play a pivotal role in electrochemical energy storage devices due to their high-power density, long cycling life, fast and stable energy storage capabilities.^[1,2] However, their relatively low energy density limits large-scale applications. Asymmetric/hybrid supercapacitors have been developed by integrating electrochemical double-layer capacitor/pseudocapacitor materials to improve the energy density.^[3–5] Electrochemical reactions predominantly occur at the electrode–electrolyte interface, involving processes such as ion adsorption/desorption, surface redox reactions, and ion intercalation/de-intercalation within the electrode material. Therefore, developing high-performance electrode materials is critical for achieving high energy density and power density in electrochemical energy storage devices.

Layered double hydroxides (LDHs), as conversion-type electrode materials, possess a high theoretical capacity (>2000 F g⁻¹).^[6–9] The adjustability of metal cations and interlayer anions endows LDHs with rich electrochemical properties,

establishing them as an ideal hybrid electrode material. Compared to single transition metal hydroxides, LDHs have an adjustable electronic state density and a reduced band gap.^[10] Nonetheless, some defects persist that restrict their performance in electrochemical energy storage applications. For instance, the low electrical conductivity of LDHs restricts their electrochemical performance, exacerbating the charge transfer limitations at high reaction rates and leading to subpar rate performance. This issue becomes more pronounced with higher loading, making it difficult for high-loading electrodes to perform effectively.^[11,12] Secondly, the α-phase hydrotalcite structure provides a larger interlayer spacing and higher capacity, which is easily transformed into the β-phase brucite structure during the electrochemical cycle. This transformation leads to decreased electrochemical performance and poor cycle stability.^[13,14] To solve these problems, several feasible solutions have been proposed in recent research work to overcome these difficulties, including interlayer anion engineering,^[15–17] heterogeneous structure composite engineering,^[18–20] ternary LDH,^[21–25] defect engineering and doping, and so on.^[26–28]

Various hierarchical structures between the metal or metal oxide layers and LDH heterostructured composite electrodes have been constructed, including Ni,^[29,30] Mn,^[31] Al,^[32] Zn,^[33] and CuO.^[19] Among them, the arrayed metals or metal oxides enhance the surface area and provide a conductive core for high-capacity LDH active materials, and the hierarchical structure of LDH endows the electrode with excellent charge transfer properties and ion diffusion capability. Li et al.^[34] prepared the composite structure of CuO and LDH materials and designed a CuO@CoFe-LDH flexible electrode with good charge transfer

M. Shao, Q. Wu, G. Tang

Northwest Minzu University School of Mathematics and Computer Science
Lanzhou, Gansu 730000, P. R. China

E-mail: jstgm@xbmu.edu.cn

M. Shao, Q. Wu, Y. Yang, F. Li, H. Sheng, J. Yuan, H. Bi, Y. Ma, H. Zhang,
W. Lan

Lanzhou University School of Physical Science and Technology
Lanzhou, Gansu 730000, China
E-mail: lanw@lzu.edu.cn



Supporting information for this article is available on the WWW under <https://doi.org/10.1002/batt.202500446>

properties and ion diffusion capacity. Moreover, doping engineering of LDH materials is an important means for enhancing their electrochemical performance. Incorporating alkali metal cations into the lattice of LDHs to substitute for transition metal elements allows for further modification of the electronic state density and optimization of the band structure. This approach reduces the band gap but also facilitates the formation of interlayer ion transport channels, thereby enhancing both conductivity and stability. Alternatively, the exchange of interlayer anions can expand the interlayer distance, facilitating the diffusion of hydroxide ions between the layers and stabilizing the α phase. For example, Al^{3+} , Zn^{2+} , and Cu^{2+} ions are introduced into the NiCo-LDH to form NiCoAl-LDH,^[18] NiCoZn-LDH,^[33] NiCoCu-LDH.^[35] Kim et al.^[14] discussed the electrochemical performance changes of LDH when different halogen ions Cl^- , Br^- , and I^- were used as interlayer anions. However, the controllable codoping of anions and cations to synergistically regulate interlayer ion transport and conductivity in LDHs poses a significant challenge. Moreover, relatively few reports focus on the codoping of alkali metal cations and halogen anions within the LDH structures. Therefore, it is still necessary to further optimize the electrochemical performance of LDH by adopting the synergistic effect of different strategies to simultaneously achieve high capacity, excellent rate performance, and stability at higher loadings.

Herein, we reported the $\text{CF}/\text{CuO}@\text{CoNi-LDH}_{(x,y)}$ ($x = \text{Li}^+$, Na^+ , and K^+ ; $y = \text{Cl}^-$, Br^- , and I^-) composite cathode with the synergistic effect of hierarchical structure and dual-ion doping. Specifically, CuO nanowire arrays (CuO NWAs) on the Cu foam (CF) acted as a conductive core to improve charge transfer. Meanwhile, the large specific surface area of CuO NWAs increased the loading of the active material $\text{LDH}_{(x,y)}$. Orthogonal comparative doping experiments with various alkali metal cations and halide ions were conducted to analyze the effects of different ion doping. For the $\text{LDH}_{(x,y)}$ electrodes, the smallest ionic radius of Li^+ easily enters the cation vacancies or terminal defects,

optimizing the electronic structure and enhancing charge transfer ability. The doping of halide ions introduces multiple effects, including the thermodynamic influence on OH^- adsorption energy and the kinetic impact of band tuning on the charge transfer ability, as well as the size effect on ion diffusion capability. Among them, Br^- achieves a better balance among these effects, exhibiting the best performance. Electrochemical kinetics analysis further revealed that the $\text{LDH}_{(\text{Li},\text{Br})}$ electrode exhibited optimized charge transfer and ion diffusion characteristics. At a loading amount of 16 mg cm^{-2} , an areal capacitance of 45.9 F cm^{-2} was achieved at a current density of 5 mA cm^{-2} representing a 37% increase in capacitance compared to the undoped electrode. Moreover, benefiting from ion stabilization effects, the capacitance retention rates were 65% (at 100 mA cm^{-2}) after 14 000 cycles. Beyond single-electrode performance, an asymmetric supercapacitor (ASC) device assembled with $\text{CF}/\text{CuO}@\text{CoNi-LDH}_{(\text{Li},\text{Br})}$ as the positive electrode and activated carbon (AC) as the negative electrode exhibits excellent electrochemical behavior, delivering 1.87 F cm^{-2} at 5 mA cm^{-2} , with 55.6% capacitance retention at 30 mA cm^{-2} , stable cycling performance (89.15% retention after 6400 cycles), and a high energy density of 0.67 mWh cm^{-2} . These results highlight the synergistic advantages of dual-ion doping and hierarchical architecture, offering a promising route for developing high-loading, high-performance cathode materials for practical electrochemical energy storage applications.

2. Results and Discussion

2.1. Design of the $\text{CuO}@\text{CoNi-LDH}_{(x,y)}$ Compositie Materials

The synthesis route for $\text{CuO}@\text{CoNi-LDH}_{(x,y)}$ (denoted as $\text{LDH}_{(x,y)}$, where $x = \text{Li, Na, K}$; $y = \text{Cl, Br, I}$) grown in situ on CF is illustrated in Figure 1. A hierarchical architecture is constructed between the CF/CuO and the $\text{CoNi-LDH}_{(x,y)}$, which effectively

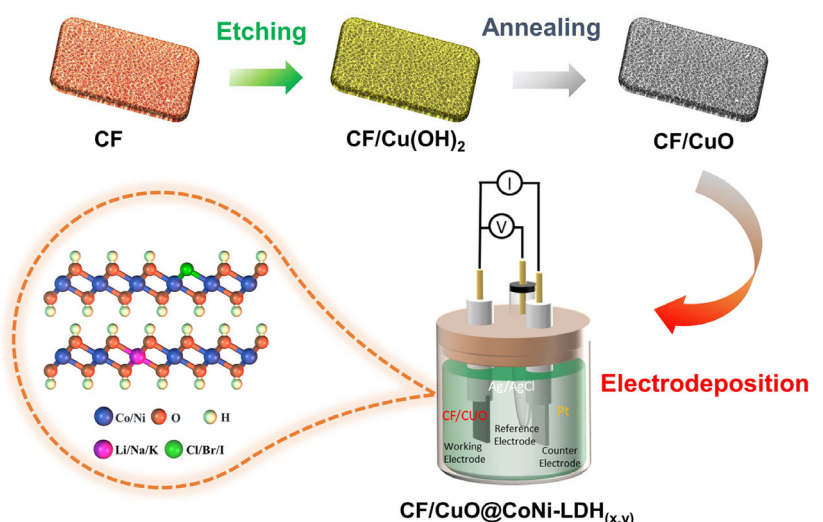


Figure 1. Schematic illustration of the prepared process for $\text{CF}/\text{CuO}@\text{CoNi-LDH}_{(x,y)}$ ($x = \text{Li, Na, K}$; $y = \text{Cl, Br, I}$) electrode materials.

increases the specific surface area and enhances active material loading. In addition, the metallic Cu core promotes efficient charge transport.

Specifically, the CF/CuO precursor is prepared through a two-step process. The CF was cleaned with hydrochloric acid to achieve hydrophilicity and then etched CF in a mixed alkaline solution with NaOH and $(\text{NH}_4)_2\text{S}_2\text{O}_8$ to obtain CF/Cu(OH)₂ NWAs, which are subsequently annealed and further transformed into CF/CuO NWAs in situ. The CoNi-LDH exhibits a typical layered double hydroxide structure, consisting of transition metal hydroxide layers and interlayer charge-balancing anions, with intercalated water molecules to maintain structural integrity.^[36–38] By adjusting the electrolyte composition during electrodeposition, alkali metal ions (Li^+ , Na^+ , K^+) can preferentially substitute Co/Ni sites, while halide ions (Cl^- , Br^- , I^-) partially replace lattice oxygen. To systematically investigate the effect of this dual-ion

doping strategy on electrochemical performance, a multivariate orthogonal experimental design was employed for optimization.

2.2. Morphological and Structural Characterization of Electrode Materials

To elucidate the effect of anion species on the material's structure, we first examined how different halide ion dopants influence the microstructure of the composite materials, with the doped cation composition kept constant. The scanning electron microscopy (SEM) images of LDH_(Li,y) with excellent electrochemical performance are shown in Figure 2a–c. The 2D vertically wrinkled LDH nanosheets, interconnected and grown on the surface of the CuO NWAs, and the hierarchical structure can still be well maintained in LDH_(Li,Cl) and LDH_(Li,Br) electrode materials, which are beneficial to the infiltration of electrolytes during the

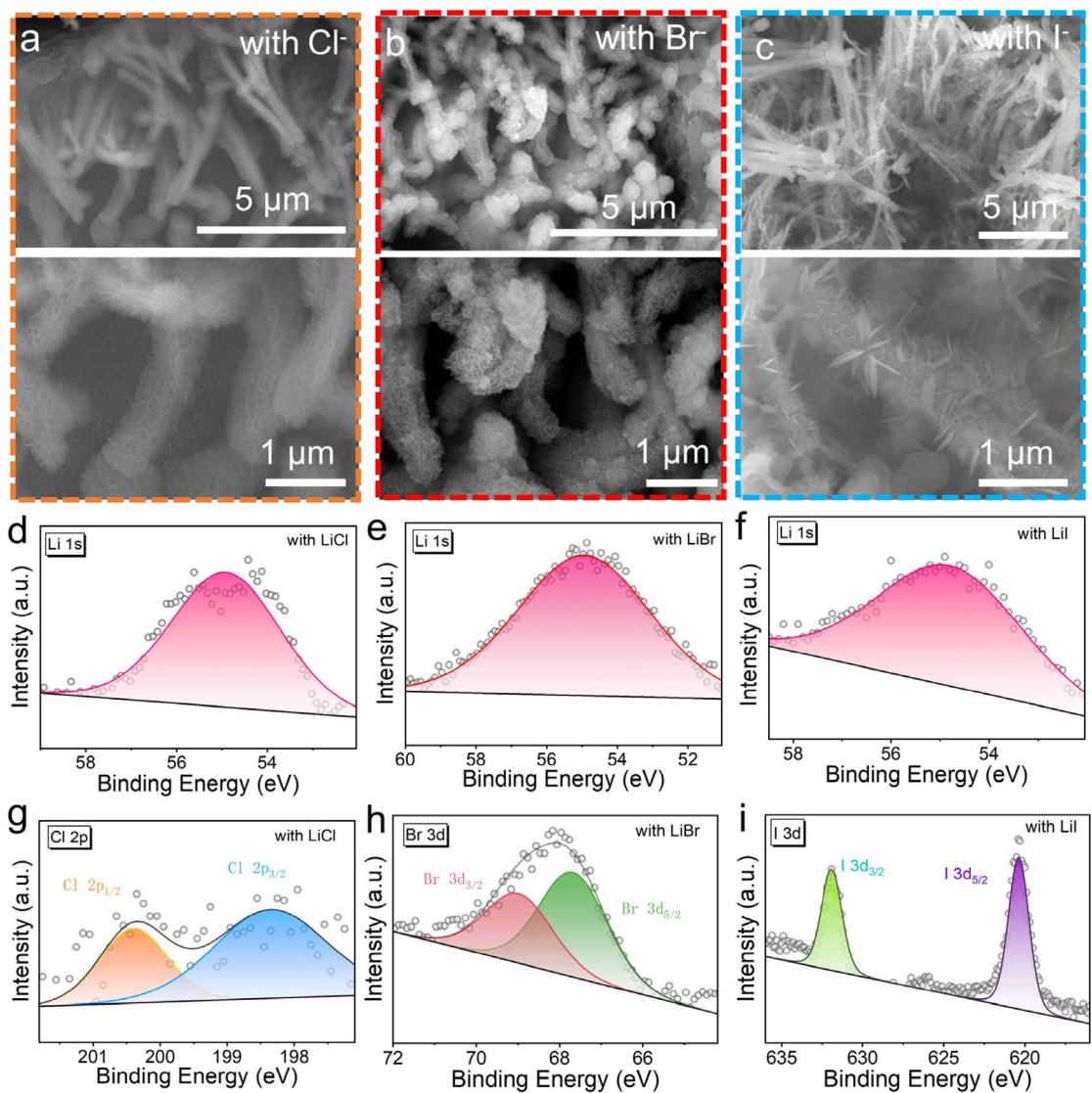


Figure 2. Morphology and structure of the CF/CuO@CoNi-LDH_(x,y). SEM images of a) CF/CuO@CoNi-LDH_(x,Cl⁻), b) CF/CuO@CoNi-LDH_(x, Br⁻), and c) CF/CuO@CoNi-LDH_(x, I⁻). The high-resolution XPS spectra of Li 1s in d) LiCl, e) LiBr, and f) LiI. The high-resolution XPS spectra of g) Cl 2p, h) Br 3d, and i) I 3d.

electrochemical reaction process and further improve ion diffusion and charge transfer. However, as shown in Figure 2c, the $\text{LDH}_{(\text{Li},\text{I})}$ electrode exhibits distinct morphological features, where needle-like LDH structures are loosely suspended on the surface of the CuO NWAs. This morphology is attributed to the large ionic radius of the I^- dopant, which induces a pronounced size effect. The expanded interlayer spacing and weakened interlayer interactions hinder grain growth, often leading to structural discontinuities around the I^- ions. In addition, the reduced number of binding sites between the LDH and CuO components disrupts the local continuity of the LDH framework. These structural deficiencies impair electronic connectivity and charge transfer pathways, ultimately leading to inferior electrochemical performance.

The amorphous nature of the LDH structure restricts the amount of structural information that can be extracted from X-ray diffraction analysis. On this basis, the high-resolution X-ray photoelectron spectroscopy (XPS) was employed to investigate the chemical composition of the anion–cation codoped LDH electrodes, including $\text{LDH}_{(\text{Li},\text{Cl})}$, $\text{LDH}_{(\text{Li},\text{Br})}$, $\text{LDH}_{(\text{Li},\text{I})}$, $\text{LDH}_{(\text{Na},\text{Br})}$, and $\text{LDH}_{(\text{K},\text{Br})}$. The peaks of Li 1s (54.9 eV) and Na 2s (63.3 eV) are clearly visible in Figure 2d–f and Figure S1a, Supporting Information, confirming Li^+ and Na^+ incorporation. Additionally, peaks at 293.0 and 295.8 eV correspond to K 2p_{3/2} and K 2p_{1/2} (Figure S1c, Supporting Information), indicating successful K^+ doping. The peaks at 198.4 and 200.3 eV (Figure 2g) are assigned to Cl 2p_{3/2} and Cl 2p_{1/2}, while Figure 2h and Figure S1b, S1d, Supporting Information show the characteristic spin-orbit doublets of Br⁻ (Br 3d_{5/2} at 68.4 eV, Br 3d_{3/2} at 69.9 eV) and I⁻ (I 3d_{5/2} at 620.4 eV, I 3d_{3/2} at

613.9 eV), confirming the presence of halide ions in the LDH structure. Overall, these results demonstrate the successful and scalable incorporation of various alkali metal cations and halide anions into the LDH matrix via electrochemical deposition.

2.3. Electrochemical Performance of the $\text{CuO}@\text{CoNi-LDH}_{(\text{x},\text{y})}$ Electrodes

The electrochemical performance was carried out for CF/CuO@CoNi-LDH_(x,y) electrodes in a three-electrode configuration using 3 M KOH aqueous electrolyte with a potential window of –0.1–0.5 V. The active material loading was controlled by electrodeposited cycles, maintaining a mass of \approx 16 mg, to accurately evaluate the effect of different doping ions on the electrochemical performance. Figure 3a shows cyclic voltammetry (CV) curves of these electrodes at 0.5 mV s⁻¹ for comparison. It can be found that these CV curves of LDH_(x,y) electrodes display a pair of oxidation and reduction peaks that are similar to the CF/CuO@CoNi-LDH_(w/o) (LDH_(w/o)) electrode, and the shape of these CV curves shows no obvious difference due to the embedding of diverse ions.^[39] Notably, no significant peak separation was observed at a low scan rate. Based on our group's previous work, the feed ratio of the transition metal element was determined to be Co:Ni = 1:4, the redox peak position should be basically fixed.^[39,40] However, compared to the LDH_(w/o) electrode, the position of oxidation and reduction peaks of LDH_(x,y) electrodes moves to a higher potential, likely due to the change in the chemical environment of the metal element caused by the doping of halogens with different electronegativity.^[41,42] This was also verified

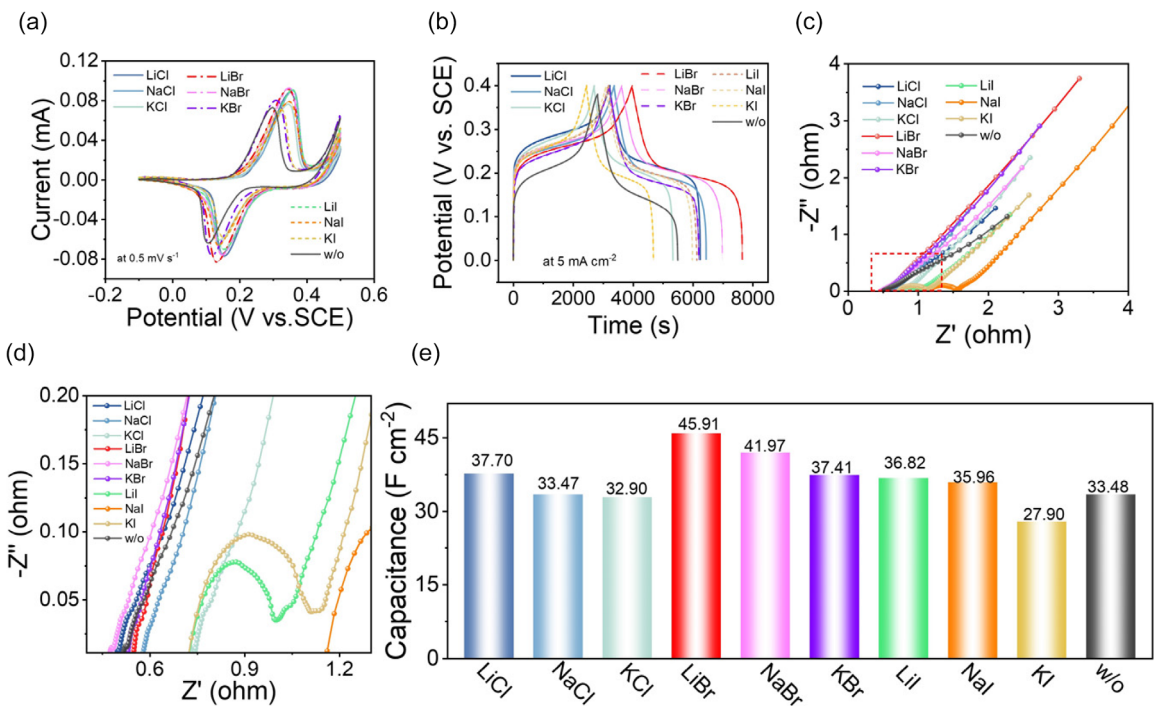


Figure 3. The electrochemical performance of CF/CuO@CoNi-LDH_(x,y) electrodes. a) The CV curves at 0.5 mV s⁻¹, b) the GCD curves at 5 mA cm⁻², c,d) the EIS curves of electrodes, and e) the calculated specific areal capacitances at 5 mA cm⁻².

by the corresponding charge/discharge (GCD) profiles at 5 mA cm^{-2} , obvious charge–discharge plateaus indicate the nature of the battery-level charge reaction in Figure 3b. The integral area of the CV curves and the charge–discharge time indicate that the $\text{LDH}_{(\text{x},\text{Br})}$ electrodes generally show higher capacity than the Cl^- ion doped and I^- ion doped electrodes. The areal capacitances of $\text{LDH}_{(\text{x},\text{y})}$ electrodes were calculated from GCD profiles at 5 mA cm^{-2} in Figure 3e. Apparently, for the electrodes with different cation doped, $\text{LDH}_{(\text{Li},\text{y})}$ electrodes present a high capacity including $\text{LDH}_{(\text{Li},\text{Cl})}$ of 37.70 F cm^{-2} , $\text{LDH}_{(\text{Li},\text{Br})}$ of 45.91 F cm^{-2} and $\text{LDH}_{(\text{Li},\text{I})}$ of 36.82 F cm^{-2} compared with $\text{LDH}_{(\text{Na},\text{y})}$ and $\text{LDH}_{(\text{K},\text{y})}$ electrodes. The $\text{LDH}_{(\text{Li},\text{Br})}$ electrode exhibits a higher capacitance with a 37% performance improvement compared to the $\text{LDH}_{(\text{w/o})}$ electrode (33.18 F cm^{-2}), owing to the smaller ionic radius of Li^+ relative to Na^+ and K^+ , which allows it to more easily occupy cation vacancies or terminal defects, optimizing the electronic structure within the material.^[18,31,43] Besides, the influence of the anions on the performance is higher than that of the cation. Especially, the doping ions including Br^- , Cl^- , and I^- ions display lower electronegativity than O^{2-} and can improve Ni-O or Co-O covalent trait on CoNi-LDH, promoting the migration of charges during the electrochemical reaction.^[17,41,42] Finally, the CF/CuO NWAs core with a high specific surface area and good conductivity improves the loading capacity and charge transfer capability to achieve excellent electrochemical performance. The electrochemical impedance spectroscopy (EIS) was used to evaluate the charge transfer and ion diffusion properties of the electrodes. As shown in Figure 3c, the $\text{LDH}_{(\text{x},\text{Br})}$ electrodes display a nearly vertical line in the low-frequency region, indicating fast ion diffusion. In Figure 3d, both $\text{LDH}_{(\text{x},\text{Br})}$ and $\text{LDH}_{(\text{x},\text{Cl})}$ exhibit low equivalent series resistance (R_s) and negligible charge transfer resistance (R_{ct}), as evidenced by the absence of a semicircle. This correlates with their compact and well-connected morphology observed in SEM images. In contrast, the $\text{LDH}_{(\text{x},\text{I})}$ electrodes exhibit a significantly higher R_s and a pronounced semicircle in the high-frequency region, indicating increased R_{ct} and poor interfacial charge transfer capability. This is consistent with the SEM observations, where the I^- -doped samples show disrupted and less interconnected LDH structures, leading to reduced electrical conductivity and diminished electrochemical performance. The adverse structural effects caused by I^- -doped outweigh the potential benefits of enhanced ion diffusion, ultimately limiting the overall electrochemical performance.

2.4. Electrochemical Kinetic Analysis of the $\text{CuO@CoNi-LDH}_{(\text{x},\text{y})}$ Electrodes

To further investigate the effect of different ion doping on the electrochemical performance of $\text{LDH}_{(\text{x},\text{y})}$ electrodes, we conducted comprehensive electrochemical tests on each electrode. Typically, CV curves are measured with low-loading $\text{LDH}_{(\text{x},\text{y})}$ electrodes, and the results are normalized based on the mass ratio. However, the electrochemical kinetic behavior shows notable differences under low and high-loading conditions.^[44,45] Hence, we utilize high-loading ($\approx 16 \text{ mg cm}^{-2}$) $\text{LDH}_{(\text{x},\text{y})}$ electrodes for

CV testing at relatively low scan rates ($0.5\text{--}5 \text{ mV s}^{-1}$) to minimize these discrepancies. As shown in Figure S2, Supporting Information, the CV shapes of the $\text{LDH}_{(\text{x},\text{y})}$ electrodes at different scan rates remained consistent, indicating good electrochemical stability and reversibility. The speed of the reversible electrochemical process of the electrode was reflected by the potential difference (ΔE_{ac}) and peak shift between redox peaks, calculated from the CV curve.^[42] The ion diffusion coefficient can be estimated to explore the electrodes with various ion-doped during the charge storage process, according to the Randles–Sevick formula:^[46,47]

$$I_p = (2.69 \times 10^5) n^{3/2} A D^{1/2} C v^{1/2} \quad (1)$$

where I_p is the peak current, and A represents the number of charges transferred and the area of the electrode. D and C are the diffusion coefficient and electrolyte concentration, respectively, and v is the scan rate. Therefore, the D value was estimated based on the linear relationship between I_p and $v^{1/2}$, as shown in Figure 4a–c. Notably, the $\text{LDH}_{(\text{x},\text{Br})}$ electrodes displayed the sharpest slope, indicating superior diffusion kinetics. Specifically, the slope of the $\text{LDH}_{(\text{Li},\text{Br})}$ electrodes reached 0.17303 and 0.14966 for the anode and cathode reactions, respectively. These enhancements are attributed to ionic codoping, which expands the interlayer spacing, facilitating electrolyte penetration and reducing the diffusion pathway to promote the reaction kinetics. Furthermore, the b -values were analyzed based on the CV curves at low scan rates. The electrode current can be divided into the surface control part and the diffusion control part based on the following equation:^[48]

$$i = k_1 v + k_2 v^{1/2} = av^b \quad (2)$$

where $k_1 v$ and $k_2 v^{1/2}$ represent the current contributed by the capacitive controlled and diffusion controlled. In Figure S4 and S5, Supporting Information, the b is obtained from the slope of the $\log i$ versus $\log v$ plot. The b -value of the $\text{LDH}_{(\text{x},\text{y})}$ series electrodes is lower than the LDH electrode (0.61 and 0.60) reported in the literature.^[39,49] This decrease is likely attributed to the reduced adsorption energy of the active sites at the end groups of the main LDH structure for OH^- ions after ion doping. As a result, more active atoms are exposed, which further enhances the diffusion-controlled capacity.^[41,50] The $\text{LDH}_{(\text{Li},\text{Br})}$ electrode achieved the highest capacity and displayed relatively high b values (the b -value of oxidation and reduction reactions are 0.58544 and 0.57384, respectively). This reveals that ion codoping plays a crucial role in improving the redox activity and kinetics of LDH electrodes.

The GCD curves at different current densities provide a broader range of reaction rates for high-loading electrodes. The GCD curves of the $\text{LDH}_{(\text{x},\text{y})}$ series electrodes were further examined at various current densities from 5 to 200 mA cm^{-2} within a voltage window of 0–0.4 V, as illustrated in Figure S7, Supporting Information. These curves show good symmetry at different current densities, achieving highly reversible electrochemical behavior and structure stability, indicating the system does not have additional side reactions after ion codoping. The areal capacitance and rate performance of the $\text{LDH}_{(\text{x},\text{y})}$ series

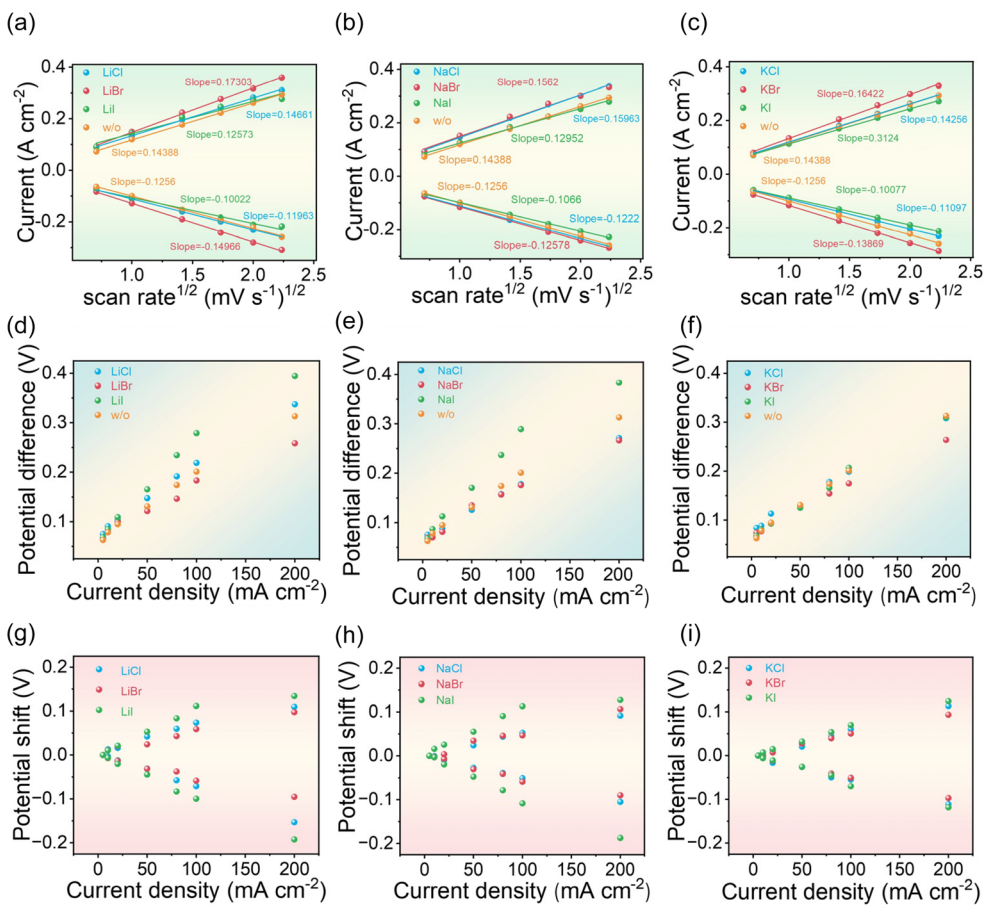


Figure 4. Electrochemical kinetics analysis of the CF/CuO@CoNi-LDH_(x,y) electrodes. The linear relationship between peak current i_p and the square root of scan rate $v^{1/2}$ of a) CF/CuO@CoNi-LDH_(Li,y), b) CF/CuO@CoNi-LDH_(Na,y), and c) CF/CuO@CoNi-LDH_(K,y). The potential difference at different current densities of d) CF/CuO@CoNi-LDH_(Li,y), e) CF/CuO@CoNi-LDH_(Na,y), and f) CF/CuO@CoNi-LDH_(K,y). The potential shifts of the cathodic and anodic peaks at different current densities of g) CF/CuO@CoNi-LDH_(Li,y), h) CF/CuO@CoNi-LDH_(Na,y), and i) CF/CuO@CoNi-LDH_(K,y).

electrodes were calculated and compared to those of undoped LDH electrodes with the same loading amount, directly illustrating the effect of ion doping on electrochemical performance (Figure S8, Supporting Information). Among the cation-doped electrodes (Li^+ , Na^+ , and K^+), the LDH_(Li,y) electrode exhibits a higher capacity. This may be attributed to the smaller size of Li^+ compared to Na^+ and K^+ , which allows easier insertion into cation vacancies or end-group defects, optimizing the electronic structure and enhancing charge transfer (Figure S8a,d,g Supporting Information).^[51–53] For anion-doped electrodes, halogen ions offer multiple benefits when substituted into the primary layer. Thermodynamically, the halogen ions replacing OH^- reduce the adsorption energy of nearby active sites for OH^- ions, exposing more active atoms.^[50,54,55] This effect weakens as the electronegativity of halogen ions gradually decreases from Cl^- to Br^- to I^- . Kinetically, halogen doping enhances the covalent nature of Co/Ni–O bonds in LDH, which is beneficial to the charge migration during electrochemical reactions. Meanwhile, halogen ion doping is beneficial to balance excess protonation, reduce polarization, and stabilize the phase structure, thereby enhancing the reversibility and rate capability of the electrochemical reaction. This aligns with the EIS results, showing greater R_s and R_{ct} values

in I⁻-doped LDH electrodes.^[41,56] In terms of ion size, the larger ion size of Cl^- , Br^- , and I^- increases interlayer distance relative to OH^- , exposing more active sites and enhancing ion diffusion capacity, consistent with the smaller ΔE_{ac} of LDH_(x,I). However, the large size of I⁻ weakens the interlayer bonding, potentially causing lattice collapse and poor rate performance (Figure S8g-i, Supporting Information). Among the anion-doped electrodes, LDH_(x,Br) provides a balanced tuning effect, achieving the highest capacity and the best rate performance. Thus, in the case of codoping, the LDH(Li,Br) electrode demonstrates optimal performance due to the synergistic effects of Li^+ and Br^- .

The differential capacitance curves of the LDH_(x,y) electrodes systematically demonstrate the differences in rate performance at different current densities (5–200 mA cm⁻²) (as shown in Figure S9, Supporting Information). The oxidation and reduction peaks of the LDH_(x,Br) and LDH_(Li,y) electrodes maintain their peak intensity, while the peak positions shift more slowly with increasing current density. This indicates that the LDH electrodes doped with Li and Br maintain good kinetic behavior during electrochemical reactions. Compared to the CV curve, the differential capacitance curve covers a broader current density range and provides a more accurate representation of the electrochemical

behavior. The ΔE_{ac} and potential shifts (shown in Figure 4d–h, respectively) were derived from the redox peaks in the differential capacitance curves. The $LDH_{(x,Br)}$ electrodes exhibit the lowest ΔE_{ac} , especially at high current density. Conversely, the $LDH_{(Li)}$ and $LDH_{(Na,I)}$ electrodes have higher ΔE_{ac} values than the $LDH_{(w/o)}$ electrodes (Figure 4d–f). This may be attributed to the low electronegativity of the I^- , leading to poor structural stability and reduced charge transfer efficiency. The ΔE_{ac} of the $LDH_{(w/o)}$ electrode exceeds 0.3 V (at 200 mA cm⁻²), while the $LDH_{(x,Br)}$ electrode remains at 0.25 V. Additionally, the $LDH_{(x,Br)}$ electrodes exhibit the smallest potential shift (at 200 mA cm⁻²), while the redox peaks potential shifting by less than 0.1 V compared to those at 5 mA cm⁻² (Figure 4g). Among the $LDH_{(x,y)}$ electrodes, the $LDH_{(Li,Br)}$ electrode exhibits the smallest potential difference and shift, indicating that the synergistic effect for codoping of Li^+ and Br^- improves both charge transfer characteristics and ion diffusion characteristics, thereby achieving superior capacitance performance and rate performance.

2.5. The $CuO@CoNi-LDH_{(Li,Br)}$ Composite Electrodes

The above analysis results indicate that the $LDH_{(Li,Br)}$ electrode, with both anion and cation codoping, exhibits excellent electrochemical performance. Consequently, the detailed structure and electrochemical performance of $LDH_{(Li,Br)}$ were further investigated in Figure 5. The morphology of the cross-linked $LDH_{(Li,Br)}$ nanosheets attached to the CuO NAWs is revealed by a transmission electron microscopy (TEM) image in Figure 5a. In contrast, a high-resolution TEM (HRTEM) image illustrates the amorphous characteristics of the LDH (Figure 5c). The selected area electron diffraction (SAED) analysis was performed on both the central and edge regions of $LDH_{(Li,Br)}$. In the central area (Figure 5b), concentric diffraction rings are observed, indicating the polycrystalline nature of the CuO in the middle of the hierarchical structure. The halo observed in the same image corresponds to the amorphous $LDH_{(Li,Br)}$. The SAED pattern from the edge area shows a simple halo ring (Figure S10, Supporting Information), further

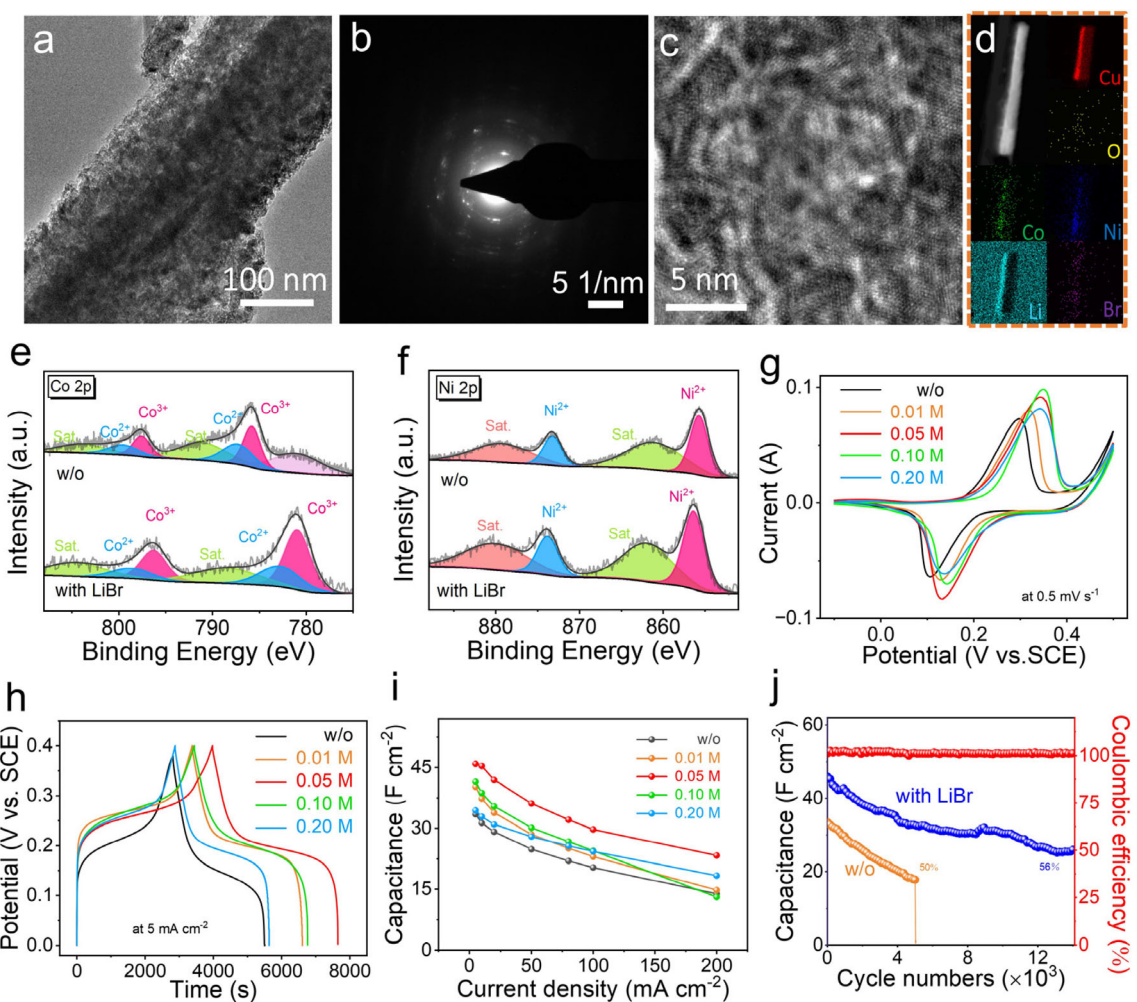


Figure 5. Morphology and electrochemical performance of the CF/CuO@CoNi-LDH_(LiBr). a) TEM, b) SAED pattern, c) high-resolution TEM image, and d) element mapping of the CF/CuO@CoNi-LDH_(LiBr) electrode. The core-level XPS spectra of e) Co 2p and f) Ni 2p of CF/CuO@CoNi-LDH_(LiBr). g) The CV curves at 0.5 mV s⁻¹, h) the GCD curves at 5 mA cm⁻², and i) the rate capability of CF/CuO@CoNi-LDH_(LiBr) electrodes with different doping concentrations. j) Electrochemical stability of CF/CuO@CoNi-LDH_(LiBr).

illustrating the amorphous structure of $\text{LDH}_{(\text{Li},\text{Br})}$. The element mapping in Figure 5d shows a uniform distribution of Cu, Co, Ni, O, Li, and Br throughout the hierarchical structure of the $\text{LDH}_{(\text{Li},\text{Br})}$. The CF/CuO acts as a conductive core to improve the electrode conductivity, while the codoping LDH structure with Li^+ and Br^- ions in the outer layer enhances the charge transport and ion migration capabilities. The synergistic effect of the hierarchical architecture contributes to the high capacity and outstanding rate performance. The XPS measurements were further performed to explore the chemical states of Cu, Co, Ni, and O elements in $\text{LDH}_{(\text{w/o})}$ and $\text{LDH}_{(\text{Li},\text{Br})}$ composites. The Cu 2p shows two main peaks at 932.1 and 951.9 eV, corresponding to metallic Cu ($\text{Cu } 2\text{p}_{3/2}$ and $\text{Cu } 2\text{p}_{1/2}$), while peaks at 933.6 and 953.65 eV correspond to the Cu^{2+} oxidation state ($\text{Cu } 2\text{p}_{3/2}$ and $\text{Cu } 2\text{p}_{1/2}$). These features confirm the coexistence of Cu and Cu^{2+} states, indicating the preserved CuO structure after Li^+/Br^- codoping (Figure S11a–c, Supporting Information). The Co 2p spectrum reveals characteristic features indicative of the coexistence of Co^{2+} and Co^{3+} species, suggesting a mixed-valence state of Co within the LDH structure. Notably, the codoped $\text{LDH}_{(\text{Li},\text{Br})}$ shows an increased Co^{3+} content compared to the $\text{LDH}_{(\text{w/o})}$. This shift is attributed to the partial substitution of OH^- by Br^- ions with a larger ionic radius, which expands the interlayer spacing, facilitates anion intercalation, and gradually leads to a weakening of the electron-withdrawing ability, resulting in a higher proportion of Co^{3+} to maintain the charge balance. In addition, the Co 2p peaks in $\text{LDH}_{(\text{Li},\text{Br})}$ exhibit a slight shift toward lower binding energy, which can be attributed to the lower electronegativity and weaker electron-withdrawing ability of Br^- compared to O^{2-} , indicating an increased electron density around Co atoms. Moreover, a portion of Co^{2+} is oxidized to Co^{3+} , which possesses higher electrical conductivity and contributes to enhanced electrochemical performance.^[37,57,58] The $\text{LDH}_{(\text{Li},\text{Br})}$ electrodes show enhanced electrical conductivity and remarkable electrochemical performance, which is consistent with the results of electrochemical tests.^[37] The XPS spectra of Ni 2p (Figure 5f) show peaks at 855.7 and 873.2 eV representing the $\text{Ni } 2\text{p}_{3/2}$ and $\text{Ni } 2\text{p}_{1/2}$, respectively.^[59,60] In addition, the O1s spectra are resolved into three peaks at 528.9, 531.1, and 532.8 eV, which are derived from metal–oxygen bonds, oxygen in the LDH (M–OH) and oxygen defects (Figure S5b–d, Supporting Information).^[42,61] There are no obvious changes in the valence state and binding energy peak position of Ni and O elements in the XPS spectra, indicating that the original structural state of the LDH material is still maintained after doping.

To clarify the advantages of dual-ion doping, a comparative study with Li^+ -doped samples was conducted. SEM images indicate that Li^+ doping induces noticeable changes in the material morphology, while EDS mapping (Figure S12, Supporting Information) confirms its uniform incorporation into the LDH structure. Electrochemical tests demonstrate that Li^+/Br^- codoped electrodes exhibit larger CV areas and longer GCD discharge times (Figure S13, Supporting Information), indicating improved capacitive behavior and charge storage. This performance enhancement is primarily attributed to the synergistic effect of Li^+ and Br^- codoping, which facilitates faster ion

transport and optimizes the local electronic structure, thereby improving the electrochemical reaction kinetics and rate performance of the material.

The electrochemical performance of the $\text{LDH}_{(\text{x},\text{y})}$ was systematically investigated through an orthogonal experiment, which led to the identification of the $\text{LDH}_{(\text{Li},\text{Br})}$ electrode with the most doping effect. Thereby, we further explored the effect of different concentrations of alkali metal and halogen ions codoped on the performance of the $\text{LDH}_{(\text{Li},\text{Br})}$ electrode. The CV curves of electrodes with different doping concentrations at 0.5 mV s⁻¹ are shown in Figure 5g. The position of both oxidation and reduction peaks overall movement to a higher potential with increasing codoping concentration. The position of redox peaks has been relatively fixed when the doped concentration increases to 0.05 M and higher, indicating that the potential for suitable substitutional doping in the electrode has reached a state of relative saturation. This trend was further verified by the GCD curves in Figure 5h. The rate capability collected from the GCD curves is shown in Figure 5i. The electrode doped with 0.05 M concentration exhibits the best rate performance, achieving a capacitance retention of 65% at 100 mA cm⁻² and 51% at 200 mA cm⁻². The doping concentration beyond 0.05 M does not improve the electrode's performance, as higher doping levels do not further reduce the OH^- adsorption energy, expand the interlayer, or optimize the electronic structure. Therefore, excessive doping leads to a reduction in the number of active sites, negatively affecting electrochemical performance. In addition to doping, the hierarchical CuO@CoNi-LDH structure significantly enhances electrochemical performance. The vertically aligned CuO nanowires on Cu foam serve as a conductive scaffold for efficient electron transport and reduced internal resistance. Their high surface area supports greater LDH loading and stable architecture, while also shortening ion diffusion paths and improving electrolyte accessibility, thereby enhancing rate capability and overall electrode durability.

The cycle stability of the $\text{LDH}_{(\text{Li},\text{Br})}$ electrode with 0.05 M doping concentration was systematically investigated (Figure 5j). After 14 000 cycles, the electrode still maintained 56% of its initial capacitance (26 F cm⁻²), which is significantly higher than the 50% capacitance retention of the LDH electrode after 5000 cycles. This substantial enhancement in cycling stability is ascribed to the improved ion diffusion kinetics, the modulation of the local electronic environment, and the stabilization of the crystal structure resulting from Li^+/Br^- codoping.^[36,42,50] Table S1, Supporting Information provides comparison results of mass loading, areal capacitance, rate performance, and cycle stability in this work and those previously reported LDH-based electrodes. By contrast, we have successfully prepared LDH-based electrode materials with high-loading, high capacity, high rate performance, and excellent cycle stability. Additionally, the coulombic efficiency of the electrode can reach 100% during the entire cycle, proving that after being doped with alkali metal ions and halogen ions, the electrode had no other side reactions and had good charge and discharge reversibility.

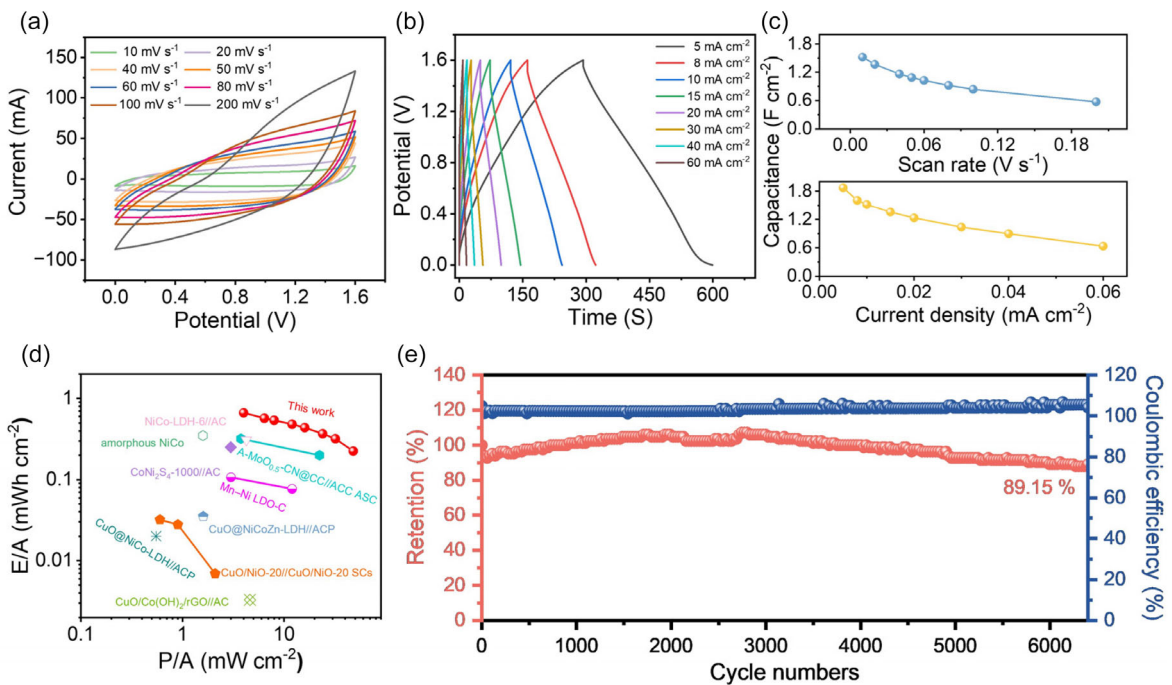


Figure 6. Electrochemical properties of the CF/CuO@CoNi-LDH_(LiBr)//AC ASC. a) The CV curves at various scan rates, b) GCD curves at various current densities, and c) rate capability of the supercapacitor. d) Ragone plot of CF/CuO@CoNi-LDH_(LiBr)//AC ASC. e) Electrochemical stability at 25 mA cm⁻².

2.6. The CuO@CoNi-LDH_(Li,Br)//AC Asymmetric Supercapacitor

To evaluate the practical applicability of the electrode, an ASC device was assembled using CF/CuO@CoNi-LDH_(LiBr) as the positive electrode and AC as the negative electrode. The electrochemical behavior of the individual electrodes was first evaluated via CV at a scan rate of 0.5 mV s⁻¹ (Figure S14a, Supporting Information), where the positive and negative electrodes exhibit distinct and complementary potential windows. This complementary behavior enables the full device to operate over an extended voltage range. As shown in Figure S14b-d, Supporting Information, the assembled ASC exhibits stable CV and GCD profiles within the voltage range of 0–1.6 V, reflecting efficient charge storage behavior. Although the device remains electrochemically active up to 1.7 V, a slight increase in polarization and a marginal decline in coulombic efficiency (99.6%) indicate the possible onset of side reactions. Consequently, 0–1.6 V was selected as the optimal operating window to ensure reliable electrochemical performance and structural stability. The assembled device exhibits stable CV curves with negligible distortion over a wide scan rate range (5–200 mV s⁻¹), indicating ideal capacitive characteristics and excellent charge transport behavior (Figure 6a). The GCD profiles recorded at various current densities (Figure 6b) display highly symmetrical triangular shapes, suggesting excellent electrochemical reversibility and low internal resistance. The device achieves a high areal capacitance of 1.87 F cm⁻² at 5 mA cm⁻² and retains 55.6% of its initial capacitance even at a high current density of 30 mA cm⁻², demonstrating

favorable rate performance (Figure 6c). Furthermore, long-term cycling stability was evaluated at 25 mA cm⁻². As shown in Figure 6e, the device maintains 89.15% of its initial capacitance after 6400 cycles, accompanied by a high coulombic efficiency of ≈97%, highlighting its excellent cycling durability and structural integrity.

The energy and power densities of the assembled device were calculated from the GCD curves, and the resulting the Ragone plot is shown in Figure 6d. The device delivers an impressive energy density of 0.67 mWh cm⁻² at a power density of 4 mW cm⁻², and maintains a high power output of 48 mW cm⁻² even at an energy density of 0.22 mWh cm⁻². Compared with previously reported CuO-based materials,^[62–65] LDH-based electrodes,^[25,66–69] and various heterostructured composites used in supercapacitors, the device demonstrates superior energy–power performance (Table S2, Supporting Information). These results highlight its great potential for practical applications in high-performance energy storage devices requiring both high energy density and rapid charge–discharge capability.

3. Conclusion

In summary, we successfully developed the CF/CuO@LDH_(x,y) electrode materials with codoping alkali metal and halogen ions via electrodeposition. The CF/CuO NWAs as conductive cores, improving the conductivity of the electrode, while the large surface areas as substrate allow for high loading of LDH_(x,y) active materials. Further, systematic orthogonal experiments reveal

that the ionic size effect of the dopants effectively expands interlayer spacing and enhances ion diffusion kinetics. Concurrently, anion doping optimizes the electrode's thermodynamics and kinetics by reducing OH^- adsorption energy, increasing the exposure of active sites, and tuning the electronic structure to improve charge transfer. Specifically, the $\text{LDH}_{(\text{Li},\text{Br})}$ electrode benefits from these synergistic effects of dual-ion codoping and hierarchical architecture, resulting in significantly enhanced electrochemical performance, including increased capacitance, superior rate capability, and excellent cycling stability under high mass loading conditions. Furthermore, ASC devices assembled with $\text{LDH}_{(\text{Li},\text{Br})}$ electrodes demonstrate promising practical performance, confirming the potential of this design strategy to advance the development of high-loading, high-performance energy storage systems.

4. Experimental Section

Materials

All of the chemicals used in the experiment were directly used and without further purification. The Cu foam was purchased from Tianjin Baishi CO., Ltd. The ammonium persulfate ($(\text{NH}_4)_2\text{S}_2\text{O}_8$) was purchased from Chengdu Kelong Chemical Reagent Factory. The cobalt nitrate ($\text{Co}(\text{NO}_3)_2 \cdot 6\text{H}_2\text{O}$), nickel nitrate ($\text{Ni}(\text{NO}_3)_2 \cdot 6\text{H}_2\text{O}$), potassium chloride (KCl), sodium chloride (NaCl), lithium chloride (LiCl), lithium bromide (LiBr), potassium bromide (KBr), sodium bromide (NaBr), lithium iodide (LiI), potassium iodide (KI), lithium nitrate (LiNO_3), and sodium iodide (NaI) were purchased from Tianjin Guangfu Technology Development CO., Ltd. The sodium hydroxide (NaOH) and potassium hydroxide (KOH) were purchased from Tianjin Baishi CO., Ltd.

Preparations of CF/CuO NWAs Precursor

The CF/CuO nanowire arrays (CF/CuO NWAs) composite electrode was prepared by the following procedure. The Cu foam (1 mm of thickness) was first ultrasonically treated with dilute hydrochloric acid (HCl, 2 wt%), ethanol, and DI water for 10 min, respectively. Next, 10.67 g of NaOH was dissolved in 100 mL DI water, and then 3.04 g of $(\text{NH}_4)_2\text{S}_2\text{O}_8$ was added into the solution with further stirring. The pretreated Cu foam was then immersed in the solution for 40 min to form the $\text{Cu}(\text{OH})_2$ nanowire arrays ($\text{Cu}(\text{OH})_2$ NWAs). Afterward, the $\text{Cu}(\text{OH})_2$ NWAs were washed with ethanol and DI water and then dried in a vacuum for 30 min. Finally, the $\text{Cu}(\text{OH})_2$ NWAs were annealed in a tube furnace at 150 °C for 2 h in an air atmosphere (with a heating rate of 5 °C per minute) to obtain CuO nanowire arrays. The CuO mass loading on the Cu foam substrate was estimated by measuring the weight change before and after the formation and annealing of $\text{Cu}(\text{OH})_2$ nanowire arrays. This difference corresponds to the deposited CuO, with an average loading of $\approx 1.5 \text{ mg cm}^{-2}$.

Preparations of $\text{CF/CuO@CoNi-LDH}_{(x,y)}$

The $\text{CF/CuO@CoNi-LDH}_{(x,y)}$ electrodes with dual ions codoping (where $x = \text{Li, Na, K}$; $y = \text{Cl, Br, I}$) were prepared via the electrocuted-deposition process, using CF/CuO NWAs as the precursor. A solution of $\text{Co}(\text{NO}_3)_2 \cdot 6\text{H}_2\text{O}$ and $\text{Ni}(\text{NO}_3)_2 \cdot 6\text{H}_2\text{O}$ was prepared as an electrodeposition solution (the feed ratio of Co:Ni = 1:4) with a concentration of 0.05 M. Different alkali metal halides (KCl, NaCl, LiCl, LiBr, KBr,

NaBr, LiI, KI, and NaI) were then added to the electrodeposition solution to incorporate dual-ion doping. The electrode-deposition was carried out using a three-electrodes configuration, including CF/CuO ($10 \times 10 \text{ cm}^2$) as the working electrode, a platinum (Pt) plate as the counter electrode, and a saturated calomel electrode (SCE) as the reference electrode. Deposition is performed within a voltage window of 0.2–1.2 V at 0.05 V s $^{-1}$ for several cycles. After deposition, the electrodes were rinsed by soaking in DI and ethanol and subsequently dried at room temperature. For clarity, the undoped CF/CuO@CoNi-LDH sample was denoted as $\text{LDH}_{(\text{w/o})}$. For CoNi-LDH, electrodes subjected to varying electrodeposition cycles were thoroughly rinsed with deionized water and ethanol to eliminate residual ions, followed by drying at room temperature. The total mass of each electrode postdeposition was recorded, and the CoNi-LDH mass loading was determined by subtracting the pre-measured mass of the pristine CF/CuO electrode from the final mass. The resulting CoNi-LDH loading was consistently maintained at $\approx 16 \text{ mg cm}^{-2}$ across all samples.

Preparations of $\text{CF/CuO@CoNi-LDH}_{(x,y)}$ //AC Asymmetric Supercapacitor

Typically, the AC electrode was prepared by mixing AC, polytetrafluoroethylene (PTFE), and Super P carbon black in a weight ratio of 8:1:1 to form a homogeneous paste. The resulting paste was then coated onto graphite foil and vacuum-dried at 60 °C for 12 h. Finally, the as-prepared CF/CuO@CoNi-LDH(LiBr) electrode (positive), AC electrode (negative), and 3 m KOH electrolyte were assembled into a hybrid supercapacitor device.

Materials Characterization

The morphology and microstructure of the $\text{LDH}_{(x,y)}$ electrodes were characterized using field-emission scanning electron microscopy (Apreo S), field TEM, HRTEM, and SAED on the Tecnai F30. Additionally, the chemical composition was investigated by XPS (PHI-5702, Mg KR X-ray, 1253.6 eV).

Electrochemical Measurements

The electrochemical performances of $\text{CF/CuO@CoNi-LDH}_{(x,y)}$ electrodes were studied in a three-electrode configuration in a 3 m KOH aqueous electrolyte using the CHI660E electrochemical workstation. The CF/CuO@CoNi-LDH(x,y) electrodes, Pt, and SCE were used as the working, counter, and reference electrodes, respectively. Electrochemical testing of ASCs using a two-electrode system.

Supporting Information

Supporting Information include the XPS spectra of $\text{CF/CuO@CoNi-LDH}_{(x,y)}$, electrochemical performance of $\text{CF/CuO@CoNi-LDH}_{(x,y)}$ electrodes, the SAED pattern and XPS spectra of $\text{CF/CuO@CoNi-LDH}_{(\text{LiBr})}$, and supplementary tables (e.g., comparison of the overall performances with reported LDH-based electrodes).

Acknowledgements

This work was supported by National Natural Science Foundation of China (62374077, 62266039), the Talent

Introduction Research Project of Northwest Minzu University (grant no. xbmuyjrc2021014), the Key Project of Natural Science Foundation of Gansu Province (grant no. 24JRRA395), the Key Research and Development Projects in Gansu Province (grant no. 25YFFA030) and the Supporting Fund for Young Researchers from Lanzhou University.

Conflict of Interest

The authors declare no conflict of interest.

Author Contributions

Mingjiao Shao: conceptualization (equal); data curation (equal); formal analysis (lead); investigation (lead); methodology (lead); validation (lead); visualization (lead); writing—original draft (lead); writing—review and editing (equal). **Qiyuan Wu:** conceptualization (equal); data curation (lead); formal analysis (lead); investigation (lead); methodology (lead); validation (lead); visualization (lead); writing—original draft (equal); writing—review and editing (equal). **Yang Yang:** supervision (equal); validation (equal); visualization (supporting). **Fengfeng Li:** supervision (supporting); validation (equal); visualization (supporting); writing—review and editing (equal). **Hongwei Sheng:** supervision (equal); validation (supporting); visualization (equal); writing—review and editing (supporting). **Jiao Yuan:** supervision (equal); validation (equal); visualization (equal). **Huasheng Bi:** supervision (equal); validation (equal); visualization (supporting). **Yuqi Ma:** validation (equal); visualization (equal). **Haoshuo Zhang:** validation (supporting); visualization (equal). **Guomei Tang:** conceptualization (lead); formal analysis (lead); funding acquisition (lead); methodology (equal); project administration (lead); resources (lead); software (lead); supervision (equal); writing—review and editing (equal). **Wei Lan:** conceptualization (lead); formal analysis (equal); funding acquisition (lead); methodology (equal); project administration (lead); resources (lead); software (lead); supervision (lead); writing—review and editing (lead).

Data Availability Statement

The data that support the findings of this study are available from the corresponding author upon reasonable request.

Keywords: cathode materials · codoping · dual-ion · hierarchical structure · layered double hydroxide

- [1] M. Winter, R. J. Brodd, *Chem. Rev.* **2004**, *104*, 4245.
- [2] Y. Zhou, H. Qi, J. Yang, Z. Bo, F. Huang, M. S. Islam, X. Lu, L. Dai, R. Amal, C. H. Wang, Z. Han, *Energy Environ. Sci.* **2021**, *14*, 1854.
- [3] Y. Shao, M. F. El-Kady, J. Sun, Y. Li, Q. Zhang, M. Zhu, H. Wang, B. Dunn, R. B. Kaner, *Chem. Rev.* **2018**, *118*, 9233.
- [4] D. Pandey, K. S. Kumar, J. Thomas, *Prog. Mater Sci.* **2024**, *141*, 101219.
- [5] D. Gao, Z. Luo, C. Liu, S. Fan, *Green Energy Environ.* **2023**, *8*, 972.
- [6] J. Yu, Q. Wang, D. O'Hare, L. Sun, *Chem. Soc. Rev.* **2017**, *46*, 5950.
- [7] S. Anantharaj, K. Karthick, S. Kundu, *Mater. Today Energy* **2017**, *6*, 1.
- [8] H. Wang, F. Sun, J. Qi, D. Zhang, H. Sun, Q. Wang, Z. Li, Y. A. Wu, Z. Hu, B. Wang, *Mater. Today Energy* **2022**, *27*, 101036.
- [9] Y. Zhang, S. Hu, C.-E. Li, X.-H. Yan, Y.-Y. Zhang, R.-B. Yin, Y.-F. Wei, K.-Z. Gao, H.-L. Gao, *Coord. Chem. Rev.* **2025**, *531*, 216497.
- [10] P. B. Jagdale, S. A. Patil, A. Sfeir, N. Barman, A. Iqbal, S. Royer, R. Thapa, A. K. Samal, D. Ghosh, M. Saxena, *Mater. Today Energy* **2024**, *44*, 101608.
- [11] G. Yilmaz, K. M. Yam, C. Zhang, H. J. Fan, G. W. Ho, *Adv. Mater.* **2017**, *29*, 1606814.
- [12] P. Thondaiman, C. J. Raj, R. Velayutham, A. D. Savariraj, R. Manikandan, V. Cristobal, B. C. Kim, *Mater. Today Energy* **2022**, *30*, 101182.
- [13] B. Zhao, L. Zhang, Q. Zhang, D. Chen, Y. Cheng, X. Deng, Y. Chen, R. Murphy, X. Xiong, B. Song, C.-P. Wong, M.-S. Wang, M. Liu, *Adv. Energy Mater.* **2018**, *8*, 1702247.
- [14] N. Kim, T.-H. Gu, D. Shin, X. Jin, H. Shin, M. G. Kim, H. Kim, S.-J. Hwang, *ACS Nano* **2021**, *15*, 8306.
- [15] Q. Pan, F. Zheng, D. Deng, B. Chen, Y. Wang, *ACS Appl. Mater. Interfaces* **2021**, *13*, 56692.
- [16] X. Han, J. Li, J. Lu, S. Luo, J. Wan, B. Li, C. Hu, X. Cheng, *Nano Energy* **2021**, *86*, 106079.
- [17] S. V. Sadavar, N. S. Padalkar, R. B. Shinde, A. S. Patil, U. M. Patil, V. V. Magdum, Y. M. Chitare, S. P. Kulkarni, S. B. Kale, R. N. Bulakhe, D. S. Bhange, S. T. Kochuveedu, J. L. Gunjakar, *Energy Storage Mater.* **2022**, *48*, 101.
- [18] K. Zhang, H.-Y. Zeng, M.-X. Wang, H.-B. Li, W. Yan, H.-B. Wang, Z.-H. Tang, *J. Mater. Chem. A* **2022**, *10*, 11213.
- [19] J.-G. Kim, H. Yu, J. Y. Jung, M. J. Kim, D.-Y. Jeon, H. S. Jeong, N. D. Kim, *Adv. Funct. Mater.* **2022**, *32*, 2113057.
- [20] J.-J. Zhou, Q. Li, C. Chen, Y.-L. Li, K. Tao, L. Han, *Chem. Eng. J.* **2018**, *350*, 551.
- [21] H. Fu, A. Zhang, F. Jin, H. Guo, J. Liu, *ACS Appl. Mater. Interfaces* **2022**, *14*, 16165.
- [22] S. C. Sekhar, G. Nagaraju, B. Ramulu, S. J. Arbaz, D. Narsimulu, S. K. Hussain, J. S. Yu, *Nano Energy* **2020**, *76*, 105016.
- [23] Q. Yang, Q. Wang, Y. Long, F. Wang, L. Wu, J. Pan, J. Han, Y. Lei, W. Shi, S. Song, *Adv. Energy Mater.* **2020**, *10*, 1903193.
- [24] Z. Liu, Y. Qiu, A. Zhang, W. Yang, C. J. Barrow, J. M. Razal, J. Liu, *J. Mater. Chem. A* **2021**, *9*, 22573.
- [25] Z. Tu, W. Tao, H. Quan, B. Tan, Z. Hong, D. Chen, *Chem. Eng. J.* **2025**, *520*, 165677.
- [26] Y. Tang, H. Shen, J. Cheng, Z. Liang, C. Qu, H. Tabassum, R. Zou, *Adv. Funct. Mater.* **2020**, *30*, 1908223.
- [27] Y. Lu, J. Guo, Z. He, Z. Gao, Y.-Y. Song, *Energy Storage Mater.* **2022**, *48*, 487.
- [28] Y. Tang, Z. Liang, Y. Jin, S. Gao, R. Zou, *J. Mater. Chem. A* **2021**, *9*, 23286.
- [29] K. M. Amin, K. Krois, F. Muench, B. J. M. Etzold, W. Ensinger, *J. Mater. Chem. A* **2022**, *10*, 12473.
- [30] K.-N. Kang, A. Ramadoss, J.-W. Min, J.-C. Yoon, D. Lee, S. J. Kang, J.-H. Jang, *Nano-Micro Lett.* **2020**, *12*, 28.
- [31] W. Guo, C. Dun, C. Yu, X. Song, F. Yang, W. Kuang, Y. Xie, S. Li, Z. Wang, J. Yu, G. Fu, J. Guo, M. A. Marcus, J. J. Urban, Q. Zhang, J. Qiu, *Nat. Commun.* **2022**, *13*, 1409.
- [32] Y. Ren, H. Du, X. Zhou, Y. Liu, Q. Wang, S. Li, W. Wang, X. Dong, *Mater. Today Energy* **2020**, *18*, 100514.
- [33] W. Hu, L. Chen, X. Wu, M. Du, Y. Song, Z. Wu, Q. Zheng, *ACS Appl. Mater. Interfaces* **2021**, *13*, 38346.
- [34] Z. Li, M. Shao, L. Zhou, R. Zhang, C. Zhang, J. Han, M. Wei, D. G. Evans, X. Duan, *Nano Energy* **2016**, *20*, 294.
- [35] N. Jayababu, D. Kim, *Small* **2021**, *17*, 2102369.
- [36] J. Ma, J. Xia, Z. Liang, X. Chen, Y. Du, C.-H. Yan, *Small* **2021**, *17*, 2104423.
- [37] X. Wang, C. Yan, A. Sumboja, J. Yan, P. S. Lee, *Adv. Energy Mater.* **2014**, *4*, 1301240.
- [38] A. Said, B. Qian, R. Zhang, C. Yang, K. Xu, K. Chen, D. Xue, *Electrochim. Acta* **2025**, *534*, 146577.
- [39] Q. Wu, F. Li, H. Sheng, Y. Qi, J. Yuan, H. Bi, W. Li, E. Xie, W. Lan, *ACS Appl. Mater. Interfaces* **2024**, *16*, 23241.
- [40] K. Wang, W. Hua, X. Huang, D. Stenzel, J. Wang, Z. Ding, Y. Cui, Q. Wang, H. Ehrenberg, B. Breitung, C. Kübel, X. Mu, *Nat. Commun.* **2023**, *14*, 1487.
- [41] Y. Qin, Q. Du, J. Deng, J. Zou, G. Lu, P. Wang, *ACS Appl. Energ. Mater.* **2022**, *5*, 469.
- [42] J. Hao, L. Yan, X. Zou, Y. Bai, Y. Han, C. Zhu, Y. Zhou, B. Xiang, *Small* **2023**, *19*, 2300467.
- [43] C. Du, S. Shi, G. Chen, Y. Zhang, Q. Wei, L. Li, G. Wan, Z. Deng, Y. Wu, Y. Su, L. Li, G. Wang, *Mater. Today Energy* **2023**, *34*, 101287.

- [44] Y. Yu, X. Hu, S. Wang, H. Qiao, Z. Liu, K. Song, X. Shen, *Nano Res.* **2022**, *15*, 685.
- [45] X. Li, D. Du, Y. Zhang, W. Xing, Q. Xue, Z. Yan, *J. Mater. Chem. A* **2017**, *5*, 15460.
- [46] M. Li, D. Yang, J. J. Biendicho, X. Han, C. Zhang, K. Liu, J. Diao, J. Li, J. Wang, M. Heggen, R. E. Dunin-Borkowski, J. Wang, G. Henkelman, J. R. Morante, J. Arbiol, S.-L. Chou, A. Cabot, *Adv. Funct. Mater.* **2022**, *32*, 2200529.
- [47] D. Yang, Z. Liang, C. Zhang, J. J. Biendicho, M. Botifoll, M. C. Spadaro, Q. Chen, M. Li, A. Ramon, A. O. Moghaddam, J. Llorca, J. Wang, J. R. Morante, J. Arbiol, S.-L. Chou, A. Cabot, *Adv. Energy Mater.* **2021**, *11*, 2101250.
- [48] L. Wang, M. Peng, J. Chen, T. Hu, K. Yuan, Y. Chen, *Adv. Mater.* **2022**, *34*, 2203744.
- [49] X. Long, Z. Wang, S. Xiao, Y. An, S. Yang, *Mater. Today* **2016**, *19*, 213.
- [50] J. Chang, S. Zhang, M. Shi, J. Feng, Z. Liu, T. Wei, Z. Fan, *Adv. Funct. Mater.* **2022**, *32*, 2109225.
- [51] R. Subbaraman, D. Tripkovic, D. Strmcnik, K.-C. Chang, M. Uchimura, A. P. Paulikas, V. Stamenkovic, N. M. Markovic, *Science* **2011**, *334*, 1256.
- [52] R. Liu, L. Chen, F. Mo, H. Song, G. Yang, C. Chen, X. Wu, Y. Huang, Z. Fan, *Chem. Eng. J.* **2023**, *455*, 140545.
- [53] J. Cao, J. Li, L. Li, Y. Zhang, D. Cai, D. Chen, W. Han, *ACS Sustain. Chem. Eng.* **2019**, *7*, 10699.
- [54] N. Mahmood, M. Tahir, A. Mahmood, J. Zhu, C. Cao, Y. Hou, *Nano Energy* **2015**, *11*, 267.
- [55] R. S. Mulliken, *J. Chem. Phys.* **1934**, *2*, 782.
- [56] J. Liu, D. Wang, K. Huang, J. Dong, J. Liao, S. Dai, X. Tang, M. Yan, H. Gong, J. Liu, Z. Gong, R. Liu, C. Cui, G. Ye, X. Zou, H. Fei, *ACS Nano* **2021**, *15*, 18125.
- [57] S.-H. Baek, Y.-M. Jeong, D. Y. Kim, I.-K. Park, *Chem. Eng. J.* **2020**, *393*, 124713.
- [58] P. Chen, T. Zhou, S. Wang, N. Zhang, Y. Tong, H. Ju, W. Chu, C. Wu, Y. Xie, *Angew. Chem., Int. Ed.* **2018**, *57*, 15471.
- [59] X. Ma, L. Zhang, G. Xu, C. Zhang, H. Song, Y. He, C. Zhang, D. Jia, *Chem. Eng. J.* **2017**, *320*, 22.
- [60] C. Liu, H. Ma, M. Yuan, Z. Yu, J. Li, K. Shi, Z. Liang, Y. Yang, T. Zhu, G. Sun, H. Li, S. Ma, *Electrochim. Acta* **2018**, *286*, 195.
- [61] H. Sheng, J. Zhou, B. Li, Y. He, X. Zhang, J. Liang, J. Zhou, Q. Su, E. Xie, W. Lan, K. Wang, C. Yu, *Sci. Adv.* **2021**, *7*, eabe3097.
- [62] X. Huang, R. Yang, H. Yin, Y. Mo, X. Shi, W. Li, S. Dai, A. Qin, K. Zhang, *J. Energy Storage* **2023**, *74*, 109319.
- [63] W. Lan, X. Zhang, A. Zhai, W. Meng, H. Sheng, W. Dou, C. Zhang, Q. Su, J. Zhou, E. Xie, *Chem. Eng. J.* **2019**, *374*, 181.
- [64] S. Xiao, L. Tian, B. Liu, J. Ding, M. Ali, Z. Xing, G. Xiao, *Mater. Res. Bull.* **2024**, *180*, 113012.
- [65] Y. Mo, X. Huang, X. Shi, W. Li, K. Zhang, A. Qin, S. Chen, *J. Alloy. Compd.* **2025**, *1017*, 179131.
- [66] S. Jiang, Y. Qiao, T. Fu, W. Peng, T. Yu, B. Yang, R. Xia, M. Gao, *ACS Appl. Mater. Interfaces* **2021**, *13*, 34374.
- [67] Q. Chen, Z. Wu, L. Zhu, C. Li, X. Zhu, Y. Sun, *J. Mater. Chem. A* **2024**, *12*, 1816.
- [68] K. A. Owusu, Z. Wang, A. Saad, F. O. Boakye, M. A. Mushtaq, M. Tahir, G. Yasin, D. Liu, Z. Peng, X. Cai, *Energy Environ. Mater.* **2024**, *7*, e12545.
- [69] X. Wang, Y. Zhang, X. Song, J. Gao, Y. Liu, S. Yang, *Electrochim. Acta* **2024**, *497*, 144514.

Manuscript received: June 10, 2025

Revised manuscript received: August 10, 2025

Version of record online: